Acta Cryst A FOUNDATIONS ADVANCES

ISSN 2053-2733

# Thermodynamics of lattice vibrations in non-cubic crystals: the zinc structure revisited

**Roman Tomaschitz***

Sechsschimmelgasse 1/21-22, Vienna, 1090, Austria. *Correspondence e-mail: tom@geminga.org

Received 23 March 2021
Accepted 26 May 2021

Edited by A. Altomare, Institute of Crystallography - CNR, Bari, Italy

**Keywords:** anisotropic lattice vibrations; thermodynamic functions; Debye–Waller factors; non-cubic crystals; temperature-dependent spectral cutoff; directional Debye temperatures; effective phonon speed; oscillator mass; heat capacity; zero-point energy.

A phenomenological model of anisotropic lattice vibrations is proposed, using a temperature-dependent spectral cutoff and varying Debye temperatures for the vibrational normal components. The internal lattice energy, entropy and Debye–Waller $B$ factors of non-cubic elemental crystals are derived. The formalism developed is non-perturbative, based on temperature-dependent linear dispersion relations for the normal modes. The Debye temperatures of the vibrational normal components differ in anisotropic crystals; their temperature dependence and the varying spectral cutoff can be inferred from the experimental lattice heat capacity and $B$ factors by least-squares regression. The zero-point internal energy of the phonons is related to the low-temperature limits of the mean-squared vibrational amplitudes of the lattice measured by X-ray and $\gamma$-ray diffraction. A specific example is discussed, the thermodynamic variables of the hexagonal close-packed zinc structure, including the temperature evolution of the $B$ factors of zinc. In this case, the lattice vibrations are partitioned into axial and basal normal components, which admit largely differing $B$ factors and Debye temperatures. The second-order $B$ factors defining the non-Gaussian contribution to the Debye–Waller damping factors of zinc are obtained as well. Anharmonicity of the oscillator potential and deviations from the uniform phonon frequency distribution of the Debye theory are modeled effectively by the temperature dependence of the spectral cutoff and Debye temperatures.

## 1. Introduction

The aim is to develop an effective theory of lattice vibrations in anisotropic crystals that can accurately reproduce the empirical thermodynamic functions and temperature evolution of Debye–Waller $B$ factors. This is motivated by the fact that the standard Debye theory usually fails to model the extended phonon peak in the lattice heat capacity of non-cubic crystals, which emerges in the crossover region between the low- and high-temperature regimes. Moreover, the Debye temperatures inferred from X-ray diffraction measurements of the mean-squared atomic displacements differ from those obtained from the low-temperature heat capacity, resulting in different X-ray and caloric Debye temperatures (*cf. e.g.* Gopal, 1966; Butt *et al.*, 1988; Peng *et al.*, 1996, 2004), which should be identical in a self-consistent theory of lattice vibrations. The linear high-temperature scaling of the $B$ factors predicted by the Debye theory is also not shown empirically, underestimating the measured factors (*cf. e.g.* Killean & Lisher, 1975; Martin & O'Connor, 1978*a*,*b*; Shepard *et al.*, 1998; Malica & Dal Corso, 2019).

A frequently used method to model empirical deviations from the Debye theory is to employ a temperature-dependent

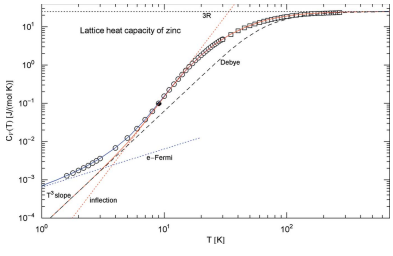

Debye temperature $\theta(T)$ in the thermodynamic functions, to be determined from measured heat capacities or Debye–Waller $B$ factors (*cf. e.g.* Barron & Munn, 1967*b*; Martin, 1968; Skelton & Katz, 1968). As is the case with constant Debye temperatures, the $\theta(T)$ functions obtained from caloric and diffraction experiments differ. Moreover, a phonon partition function with varying Debye temperature does not define an equilibrium system, since the equilibrium condition $\partial S/\partial U = 1/T$ on the internal-energy derivative of entropy is violated once the Debye temperature becomes temperature dependent (Tomaschitz, 2020*a*). Nevertheless, the idea of using a varying Debye temperature to account for deviations from the standard Debye theory is attractive because of its relative technical simplicity, avoiding perturbative expansions. Alternative attempts to adapt the Debye theory to reality include the addition of anharmonic terms to the oscillator potential (*cf. e.g.* Merisalo & Larsen, 1977, 1979; Field, 1983; Rossmanith, 1984; Kumpat & Rossmanith, 1990) and/or a modification of the continuous and uniform phonon density of states assumed in the Debye theory (*cf. e.g.* Gopal, 1966; Meissner *et al.*, 1978).

Here, we will discuss thermal vibrations of the hexagonal close-packed zinc structure (Altmann & Bradley, 1965), as an example of an anisotropic elemental crystal. The equilibrium relation $\partial S/\partial U = 1/T$ can be maintained with varying Debye temperatures $\theta_j(T)$ for the normal vibrations, provided that the spectral cutoff $\Lambda(T)$ of the thermodynamic functions is also allowed to vary with temperature. (In anisotropic crystals, the vibrational normal components admit different Debye temperatures labeled by $j$, which coincide in the case of cubic monatomic crystals.) The empirical $B$ factors and heat capacity can be described with the same set of functions $\theta_j(T)$ and $\Lambda(T)$ so that X-ray and caloric Debye temperatures coincide. The starting point in Section 2.1 will be a partition of the atomic oscillations into vibrational normal components, each component being described by a temperature-dependent Debye temperature and spectral cutoff. The varying spectral cutoff and Debye temperature of each normal component can be extracted from empirical heat capacity data by least-squares regression and from the zero-temperature limits of measured $B$ factors.

Once the directional Debye temperatures and the spectral cutoff are known, one can calculate the effective phonon speed determining the dispersion relation of each normal component, which suffices to calculate the thermodynamic functions. The temperature evolution of the effective oscillator mass of the normal vibrations can also be determined from the empirical $B$ factors. We will explain the general formalism for anisotropic monatomic crystals and work out a specific example, the thermodynamic functions and $B$ factors of zinc.

This paper is organized as follows. In Section 2.1, we discuss the lattice internal energy, entropy and the mean-squared vibrational amplitudes, the partitioning of atomic vibrations into normal components, and the partial energies and entropies and $B$ factors of the normal vibrations.

In Section 2.2, the temperature-dependent spectral cutoff and Debye temperatures of the vibrational normal components are derived. The partial oscillator density and effective phonon speed of each normal component are inferred from the respective Debye temperature and spectral cutoff. In this section and the Appendix, we explain the regression of the varying Debye temperatures and spectral cutoff from heat capacity data and empirical $B$ factors.

In Section 3, we consider Debye–Waller $B$ factors of anisotropic elemental crystals defined by the mean-squared amplitudes of the orthogonal normal vibrations. The zero-point lattice energy can be obtained from the zero-temperature limits of three $B$ factors measured by X-ray diffraction and from the amplitude of the cubic low-temperature scaling of the isochoric heat capacity. The reasoning in Sections 2 and 3 applies to anisotropic elemental crystals in general.

In Section 4, the thermodynamic variables and mean-squared vibrational amplitudes of the zinc structure are studied. Heat capacity measurements of zinc continuously extend from the low-temperature regime up to the melting point (Seidel & Keesom, 1958; Phillips, 1958; Eichenauer & Schulze, 1959; Garland & Silverman, 1961; Zimmerman & Crane, 1962; Martin, 1968, 1969; Cetas *et al.*, 1969; Mizutani, 1971; Grønvold & Stølen, 2002), converted from isobaric to isochoric values (Barron & Munn, 1967*b*; Arblaster, 2018), and $B$ factors of vibrations in the basal plane and along the hexagonal axis have also been measured over a wide temperature range [see Skelton & Katz (1968), Albanese *et al.* (1976), Pathak & Desai (1981) and earlier measurements reviewed by Barron & Munn (1967*a*) and Rossmanith (1977)]. We model the lattice heat capacity of the zinc structure with a multiply broken power-law density (Tomaschitz, 2020*a*,*b*, 2021*b*,*c*) and perform a least-squares fit to the isochoric data sets, subtracting the electronic heat capacity (*cf.* Section 4.1).

Analytic least-squares fits are also performed to the measured $B$ factors of zinc, up to the melting point (*cf.* Section 4.2). The amplitude of the low-temperature lattice heat capacity and the zero-temperature limits of the regressed $B$ factors allow us to estimate the zero-point internal energy of the zinc structure (*cf.* Section 4.3). Integrations of the regressed lattice heat capacity give the thermal components of the internal energy and the entropy (*cf.* Section 4.6). Based on these empirical functions and the zero-temperature limits of the axial and basal $B$ factors of zinc, one can determine the varying Debye temperatures of normal vibrations orthogonal and parallel to the basal plane as well as the temperature-dependent spectral cutoff (*cf.* Sections 4.4 and 4.5). Using this input, the effective phonon speed defining the dispersion relations of the normal vibrations can be calculated (*cf.* Section 4.7). The effective oscillator mass of the normal vibrations is inferred from the temperature evolution of the regressed $B$ factors (*cf.* Section 4.8). Second-order $B$ factors defining the non-Gaussian correction of the Debye–Waller damping factors are derived in Section 4.9. Section 5 contains the conclusions.

## 2. Varying Debye temperatures and spectral cutoffs of non-cubic elemental crystals

### 2.1. Lattice internal energy, entropy and mean-squared vibrational amplitudes

We consider anisotropic (*i.e.* non-cubic) monatomic crystals and split the molar internal energy of the lattice vibrations into three components, corresponding to atomic normal vibrations, $U = \sum_{j=1}^{3} U_j$,

$$U_j(T) = \frac{4\pi}{(2\pi)^3} R \frac{\Lambda^3(T)}{n_{\rm at}} T \left\{ D\left[\frac{\theta_j(T)}{T}\right] + \frac{1}{8}\frac{\theta_j(T)}{T} \right\},$$
$$D(x) := \frac{1}{x^3}\int_0^x \frac{t^3\,{\rm d}t}{\exp(t)-1}, \qquad (1)$$

where $R$ = 8.314 J (K mol)$^{-1}$ is the gas constant, the $\theta_j(T)$ are varying Debye temperatures, $\Lambda(T)$ (cm$^{-1}$) is the temperature-dependent spectral cutoff and $n_{\rm at}$ (cm$^{-3}$) the atomic density (Tomaschitz, 2020*a*, 2021*a*). The energy components $U_j(T)$ are in units of J mol$^{-1}$. $D(x)$ denotes the Debye function, with asymptotic limits $D(x\to 0)\sim 1/3$ and $D(x\to\infty)\sim \pi^4/(15x^3)$. The coordinate system defining the normal oscillations can be arbitrarily chosen; in the case of zinc, one will conveniently choose the hexagonal axis and two perpendicular axes in the basal plane. The standard Debye internal energy is recovered by assuming a constant Debye temperature $\theta_j(T) = \theta_{\rm D}$ and constant spectral cutoff, $\Lambda(T) = \Lambda_{\rm D} = (6\pi^2 n_{\rm at})^{1/3}$. The spectral representation of the partial energies (1) reads

$$\frac{U_j}{V} = \frac{4\pi}{(2\pi)^3}\int_0^{\Lambda(T)} \hbar\omega_{j,\mathbf{k}}(T) \times \left\{ \frac{1}{\exp[\hbar\omega_{j,\mathbf{k}}(T)/(k_{\rm B}T)]-1} + \frac{1}{2} \right\} k^2\,{\rm d}k, \qquad (2)$$

where the temperature-dependent linear dispersion relations $\omega_{j,\mathbf{k}} = c_{{\rm eff},j}(T)k$ are determined by the effective phonon speed $c_{{\rm eff},j} = k_{\rm B}\theta_j(T)/[\hbar\Lambda(T)]$ of the normal vibrations (labeled by subscript $j = 1, 2, 3$). The conversion of the specific energy densities $U_j/V$ in (2) to molar quantities (1) is done by multiplying (2) with $V$/mol and using $n_{\rm at} = N_{\rm A}{\rm mol}/V$ and $R = N_{\rm A}k_{\rm B}$.

The entropy can likewise be decomposed into normal components $S = \sum_j S_j$, with partial entropies

$$S_j(T) = \frac{4\pi}{(2\pi)^3} R \frac{\Lambda^3(T)}{n_{\rm at}} \times \left( \frac{4}{3} D\left[\frac{\theta_j(T)}{T}\right] - \frac{1}{3}\log\{1-\exp[-\theta_j(T)/T]\} \right). \qquad (3)$$

The temperature-dependent effective oscillator density is $n_{\rm oscil}(T) = [4\pi/(2\pi)^3]\Lambda^3(T)$, with partial densities $n_{{\rm oscil},j} = n_{\rm oscil}(T)/3$ generating the energy and entropy components in (1) and (3). The partition function is assembled as $k_{\rm B}\log Z = S - U/T$ and the Helmholtz free energy as $F = -k_{\rm B}T\log Z$.

The mean-squared displacement $\langle u_j^2(T)\rangle$ (cm$^2$) of the normal oscillators vibrating parallel to coordinate axes labeled $j$ reads (Tomaschitz, 2020*a*)

$$\langle u_j^2(T)\rangle = \frac{3}{m_{{\rm eff},j}(T)}\frac{\hbar^2 T}{k_{\rm B}\theta_j^2(T)}\left\{ D_1\left[\frac{\theta_j(T)}{T}\right] + \frac{1}{4}\frac{\theta_j(T)}{T}\right\},$$
$$D_1(x) := \frac{1}{x}\int_0^x \frac{t\,{\rm d}t}{\exp(t)-1}, \qquad (4)$$

where $m_{{\rm eff},j}(T)$ is the temperature-dependent effective oscillator mass. The corresponding Debye–Waller $B$ factors are $B_j = 8\pi^2\langle u_j^2(T)\rangle$. The asymptotic limits of the Debye function in (4) are $D_1(x\to 0)\sim 1$ and $D_1(x\to\infty)\sim \pi^2/(6x)$. A derivation of (1)–(4) based on an effective field theory for the normal oscillations can be found in Tomaschitz (2021*a*). Here, the focus is on the practical application to zinc.

### 2.2. Temperature dependence of the Debye temperatures and spectral cutoff

The lattice internal energy and entropy are related to the lattice heat capacity $C_V(T)$ [in units of J (K mol)$^{-1}$] by $U(T) = \int_0^T C_V(T)\,{\rm d}T + U_0$ and $S(T) = \int_0^T C_V(T)/T\,{\rm d}T$, respectively, where the zero-point internal energy $U_0$ is an integration constant. In Section 4.1, an analytic representation of $C_V(T)$ will be obtained from a least-squares fit of a multiply broken power-law density to heat capacity data of zinc. The analytic fit can then be integrated as indicated to find the internal energy and entropy. The zero-point energy $U_0$ will be determined from X-ray and $\gamma$-ray diffraction measurements of Debye–Waller $B$ factors (*cf.* Section 4.2).

We specialize the Debye temperatures of the normal oscillations in (1)–(4) as $\theta_j(T) = \hat{c}_j\theta(T)$, where the $\hat{c}_j$ are positive temperature-independent constants. This ansatz is sufficiently general to model anisotropic vibrations of elemental crystals. The effective phonon speed of the normal oscillations is $c_{{\rm eff},j} = \hat{c}_j c_{\rm eff}$, with $c_{\rm eff} = k_{\rm B}\theta(T)/[\hbar\Lambda(T)]$ [*cf.* after (2)].

Once $U(T)$ and $S(T)$ are extracted from the empirical heat capacity and $B$ factors, the varying Debye temperature $\theta(T)$ can be found by combining equations (1) and (3),

$$\frac{3}{4}\frac{TS(T)}{U(T)} = \Delta(d),\ \Delta(d) := \frac{\sum_j\{4D(\hat{c}_j d) - \log[1-\exp(-\hat{c}_j d)]\}}{\sum_j[4D(\hat{c}_j d) + \hat{c}_j d/2]} \qquad (5)$$

where we substituted $\theta_j = \hat{c}_j\theta(T)$ and used the shortcut $d = \theta(T)/T$. In the Appendix, we will show that the $\Delta$ function (5) is monotonously decreasing on the positive real axis, from infinity to zero, for any choice of positive constants $\hat{c}_j$. It will also be necessary to explicitly invert $\Delta(d)$ in order to calculate $\theta(T)$ by solving (5), $\theta(T) = T\Delta^{-1}(\frac{3}{4}TS/U)$. The constants $\hat{c}_j$ in (5) can be obtained from zero-temperature limits of measured $B$ factors (*cf.* Sections 3 and 4), so that the numerical inversion of $\Delta(d)$ in (7) needs to be done only once; a practical inversion method is outlined in the Appendix, *cf.* after (30).

The spectral cutoff $\Lambda(T)$ in (2) is found by solving $U = \sum_j U_j$ in (1) for $\Lambda(T)$, with $\theta_j = \hat{c}_j\theta(T)$ substituted for the directional Debye temperatures. By expressing $\theta(T)$ and $\Lambda(T)$ as functions of entropy and internal energy, the equilibrium condition $\partial S/\partial U = 1/T$ mentioned in Section 1 is preserved (Tomaschitz, 2020*a*). $U(T)$ and $S(T)$ are empirical functions, obtained from the regressed heat capacity and the low-temperature limits of the regressed $B$ factors, as exemplified with zinc in Section 4.4.

## 3. Low-temperature limits of the Debye–Waller *B* factors and zero-point energy of anisotropic lattice vibrations

At low temperature, the lattice heat capacity scales as $C_V(T \to 0) \sim c_{V0}T^3$, with amplitude $c_{V0}$ obtained from a least-squares fit (*cf.* Section 4.1), so that the internal energy converges to its zero-point limit, $U(T \to 0) \sim U_0$, and the lattice entropy scales as $S(T \to 0) \sim c_{V0}T^3/3$ (*cf.* the beginning of Section 2.2). The low-temperature limit of $\Delta(d)$ in (5) reads [*cf.* (30)]

$$\Delta(d \to \infty) \sim \frac{8\pi^4}{15}\frac{1}{d^4}\frac{\sum_j 1/\hat{c}_j^3}{\sum_j \hat{c}_j}. \tag{6}$$

Substitution of the stated limits into (5) gives the zero-temperature limit of the Debye temperature $\theta(T)$,

$$\theta_{T=0} = \left(\frac{32\pi^4}{15}\frac{U_0}{c_{V0}}\frac{\sum_j \hat{c}_j^{-3}}{\sum_j \hat{c}_j}\right)^{1/4}. \tag{7}$$

The zero-temperature limit of the $B$ factors (4) reads

$$B_{j,T=0} = 8\pi^2\frac{3}{m_{\mathrm{eff},j}(0)}\frac{1}{4}\frac{\hbar^2}{k_{\mathrm{B}}\hat{c}_j\theta_{T=0}}. \tag{8}$$

Here and in (6), we used the asymptotic expansions of the Debye functions $D(x)$ and $D_1(x)$ [*cf.* after (1) and (4) and (30)]. The zero-temperature limit of the effective oscillator mass is the atomic mass, $m_{\mathrm{eff},j}(T=0) = m$. Equation (8) defines a system of three equations, labeled by $j = 1, 2, 3$, that can be solved for $\theta_{T=0}$, $\hat{c}_2$ and $\hat{c}_3$:

$$\theta_{T=0} = 6\pi^2\frac{\hbar^2}{k_{\mathrm{B}}}\frac{1}{\hat{c}_1 B_{1,T=0} m},\ \hat{c}_j = \hat{c}_1\frac{B_{1,T=0}}{B_{j,T=0}}. \tag{9}$$

We substitute this into (7) and solve for $U_0$ to find the zero-point internal energy,

$$U_0 = \frac{15}{32\pi^4}\left(\frac{\hbar^2}{k_{\mathrm{B}}}6\pi^2\right)^4\frac{c_{V0}}{m^4}\frac{\sum_j 1/B_{j,T=0}}{\sum_j B_{j,T=0}^3}, \tag{10}$$

where $c_{V0}$ is the empirical amplitude of the low-temperature lattice heat capacity, $C_V \sim c_{V0}T^3$.

One of the temperature-independent constants $\hat{c}_j$ defining the Debye temperatures $\theta_j(T) = \hat{c}_j\theta(T)$, *cf.* Section 2.2, can be absorbed into $\theta(T)$, so that we can put $\hat{c}_1 = 1$ from the outset. The remaining constants $\hat{c}_{j=2,3}$ defining the directional Debye temperatures $\theta_j$ can be inferred from the zero-temperature limits $B_{j,T=0}$ of the empirical $B$ factors by way of (9).

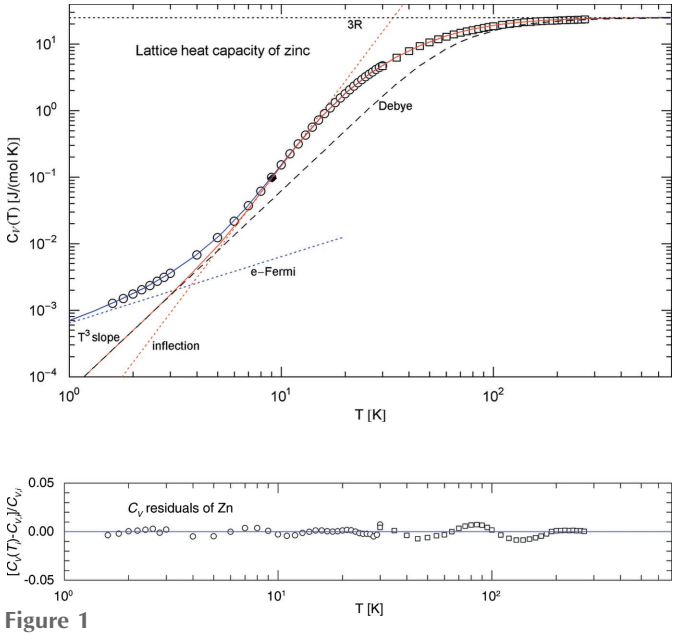


**Figure 1**
Isochoric heat capacity of zinc. Data points from Martin (1968, 1969) (circles) and Eichenauer & Schulze (1959) (squares). The least-squares $\chi^2$ fit (solid blue curve) is performed with $C_{V,\mathrm{e+L}}(T)$ in (11) (combined electronic and lattice heat capacity), the fitting parameters are stated in Table 1. The classical $3R$ Dulong–Petit limit is indicated by the black dotted horizontal line. The lattice heat capacity $C_V(T)$ of the zinc structure [red solid curve depicting the multiply broken power-law density in (11)] has a cubic low-temperature slope and is obtained from the least-squares fit $C_{V,\mathrm{e+L}}(T)$ (solid blue curve) by subtracting the linear electronic low-temperature heat capacity $b_{\mathrm{elec}}T$ (blue dotted line), *cf.* (11) and Table 1. $C_V(T)$ has an inflection point (black diamond) in log–log representation at $T_{\mathrm{inflec}} = 9.085$ K, $C_V(T_{\mathrm{inflec}}) = 0.0986$ J mol$^{-1}$; the inflection tangent $\propto T^{4.223}$ is depicted as a red dotted line. The Debye approximation $C_{V,\mathrm{D}}(T)$ (black dashed curve) with constant Debye temperature $\theta_{\mathrm{D}} = 314.79$ K, *cf.* (12), admits the same low- and high-temperature limits as $C_V(T)$ but does not have a log–log inflection point and largely deviates from the data points in the crossover regime. The maximum of the relative deviation $(C_V - C_{V,\mathrm{D}})/C_V$ of the Debye approximation from the empirical heat capacity occurs at 18.5 K, where $C_V/C_{V,\mathrm{D}} = 3.66$ and $C_V = 1.44$ J (K mol)$^{-1}$. The difference $C_V - C_{V,\mathrm{D}}$ is listed in Table 2, for selected temperatures. The temperature range is cut off at the melting point of zinc, at 692.73 K. Residuals of the $\chi^2$ fit of $C_{V,\mathrm{e+L}}(T)$ are shown in the lower panel.

## 4. Thermodynamic functions and Debye–Waller factors of zinc

### 4.1. Regressed lattice heat capacity of the zinc structure

We perform a least-squares fit to the empirical heat capacity of zinc (Eichenauer & Schulze, 1959; Martin, 1968, 1969); see also Seidel & Keesom (1958), Phillips (1958), Garland & Silverman (1961), Zimmerman & Crane (1962), Cetas *et al.* (1969), Mizutani (1971) and Grønvold & Stølen (2002) for experimental data, converted to isochoric values and depicted in the double-logarithmic plot in Fig. 1. The isochoric heat capacity $C_{V,\mathrm{e+L}}(T)$ can be split into a linear component stemming from the degenerate electron gas and a multiply broken power law (Tomaschitz, 2017, 2020*c*, 2021*b*,*c*) for the lattice heat capacity $C_V$,

**Table 1**
Fitting parameters of the isochoric heat capacity $C_{V,\mathrm{e+L}}(T)$ (electronic and lattice heat capacity) of zinc.

The recorded amplitudes $b_i$ and exponents $\beta_i$, $\eta_i$ define the multiply broken power-law density (11) used for the fit of the heat capacity in Fig. 1. (Some of the parameters are interrelated, *e.g.* $\beta_3 = 3 + \beta_1 - \beta_2$, *cf.* Section 4.1.) $b_{\mathrm{elec}}$ is the amplitude of the linear electronic power law included in the $\chi^2$ fit, *cf.* (11). The listed $\chi^2$ is the minimum of the least-squares functional $\chi^2 = \sum_{i=1}^{N}[C(T_i) - C_i]^2/C_i^2$, where $C$ is a shortcut for $C_{V,\mathrm{e+L}}$; the degrees of freedom [d.o.f.: number $N$ of data points $(T_i, C_i)$ minus number of independent fitting parameters] are also recorded. The standard error SE = $\{\sum_{i=1}^{N}[C(T_i) - C_i]^2/N\}^{1/2}$ of the fit is 0.0589. The coefficient of determination, $R^2 = 1 - \sum_{i=1}^{N}[C(T_i) - C_i]^2/(N\sigma^2)$, with sample variance $\sigma^2 = \sum_{i=1}^{N}(C_i - \bar{C})^2/N$ and mean $\bar{C} = \sum_{i=1}^{N} C_i/N$, is estimated as $1 - R^2 = 3.88 \times 10^{-5}$.

| $b_{\mathrm{elec}}$ [J (K$^2$ mol)$^{-1}$] | $b_0$ [J (K$^4$ mol)$^{-1}$] | $b_1$ (K) | $b_2$ (K) | $b_3$ (K) | $\beta_1$ | $\beta_2$ | $\eta_1$ | $\eta_2$ | $\eta_3$ | $\chi^2$ | d.o.f. |
|---|---|---|---|---|---|---|---|---|---|---|---|
| $6.3899 \times 10^{-4}$ | $6.2314 \times 10^{-5}$ | 7.4222 | 11.615 | 53.290 | 5.6567 | 6.6810 | 1.9078 | 2.7421 | 1.0039 | 0.0545 | 67 − 9 |

$$C_{V,\mathrm{e+L}}(T) = b_{\mathrm{elec}}T + C_V(T),$$
$$C_V(T) = b_0T^3[1 + (T/b_1)^{\beta_1/\eta_1}]^{\eta_1} \times \frac{1}{[1 + (T/b_2)^{\beta_2/\eta_2}]^{\eta_2}} \frac{1}{[1 + (T/b_3)^{\beta_3/\eta_3}]^{\eta_3}}. \quad (11)$$

The amplitudes $b_{\mathrm{elec}}$, $b_0$ and $b_1 < b_2 < b_3$ and the exponents $\beta_i$ and $\eta_i$ are positive and related by $b_3 = [3Rb_1^{\beta_1}/(b_2^{\beta_2}b_0)]^{1/\beta_3}$ and $\beta_3 = 3 + \beta_1 - \beta_2$, so that the classical Dulong–Petit limit $C_V(T \to \infty) \sim 3R$ is recovered, with gas constant $R$ = 8.314 J (K mol)$^{-1}$. The isochoric data points in Fig. 1 include the electronic component of the heat capacity, and the least-squares fit is done with $C_{V,\mathrm{e+L}}(T)$. The independent fitting parameters $b_{\mathrm{elec}}$, $b_{0,1,2}$, $\beta_{1,2}$, $\eta_{1,2,3}$ are recorded in Table 1. The lattice heat capacity $C_V(T)$ of the zinc structure is obtained by subtraction of the electronic contribution $b_{\mathrm{elec}}T$ from the regressed $C_{V,\mathrm{e+L}}(T)$ and has the low-temperature limit $C_V(T \to 0) \sim b_0T^3$. The units used are $C_V$ [J (K mol)$^{-1}$], $b_{\mathrm{elec}}$ [J (K$^2$ mol)$^{-1}$], $b_0$ [J (K$^4$ mol)$^{-1}$] and $b_i$ (K). The linear electronic power law in (11) is exponentially cut off at high temperature (classical regime), but in the temperature range below the melting point we do not need to consider this, since even the linear power law is dwarfed by the lattice heat capacity except, of course, in the low-temperature regime (see Fig. 1).

In contrast to the Debye heat capacity, the empirical lattice heat capacity of the zinc structure has an inflection point in log–log representation (*cf.* Fig. 1); the tangent of $C_V(T)$ at the inflection point is depicted as a red dotted line $\propto T^{4.223}$, at $T_{\mathrm{inflec}}$ = 9.085 K, $C_V(T_{\mathrm{inflec}})$ = 0.0986 J mol$^{-1}$. $C_{V,\mathrm{e+L}}(T)$ and $C_V(T)$ are plotted in Fig. 1 up to the melting point of zinc at 692.73 K.

Also shown in Fig. 1 is the Debye approximation,

$$C_{V,\mathrm{D}}(T) = 9R\left[4D(\theta_{\mathrm{D}}/T) - \frac{\theta_{\mathrm{D}}/T}{\exp(\theta_{\mathrm{D}}/T) - 1}\right],$$
$$\theta_{\mathrm{D}} = \left(\frac{12}{5}\pi^4\frac{R}{b_0}\right)^{1/3}, \quad (12)$$

with Debye function $D(d)$ in (1). The constant Debye temperature of zinc is $\theta_{\mathrm{D}}$ = 314.79 K, obtained from the low-temperature amplitude $b_0$ in (11) and Table 1. The constant effective phonon speed is $c_{\mathrm{eff,D}} = k_{\mathrm{B}}\theta_{\mathrm{D}}/(\hbar\Lambda_{\mathrm{D}})$, *cf.* after (2), with cutoff factor $\Lambda_{\mathrm{D}} = (6\pi^2n_{\mathrm{at}})^{1/3}$, *cf.* after (1), so that $c_{\mathrm{eff,D}}$ = 2.62 km s$^{-1}$, based on the atomic density $n_{\mathrm{at}} = 6.5702 \times 10^{22}$ cm$^{-3}$. The zero-point energy in the Debye model is $U_{0,\mathrm{D}} = 9R\theta_{\mathrm{D}}/8$, *cf.* (1) and (30), which gives $U_{0,\mathrm{D}}$ = 2944.5 J mol$^{-1}$ for zinc, incompatible with the zero-temperature limits of the measured $B$ factors (*cf.* Section 4.3). The empirical heat capacity of zinc has an extended phonon peak at around 20 K (*cf.* Fig. 1), which is not reproduced by

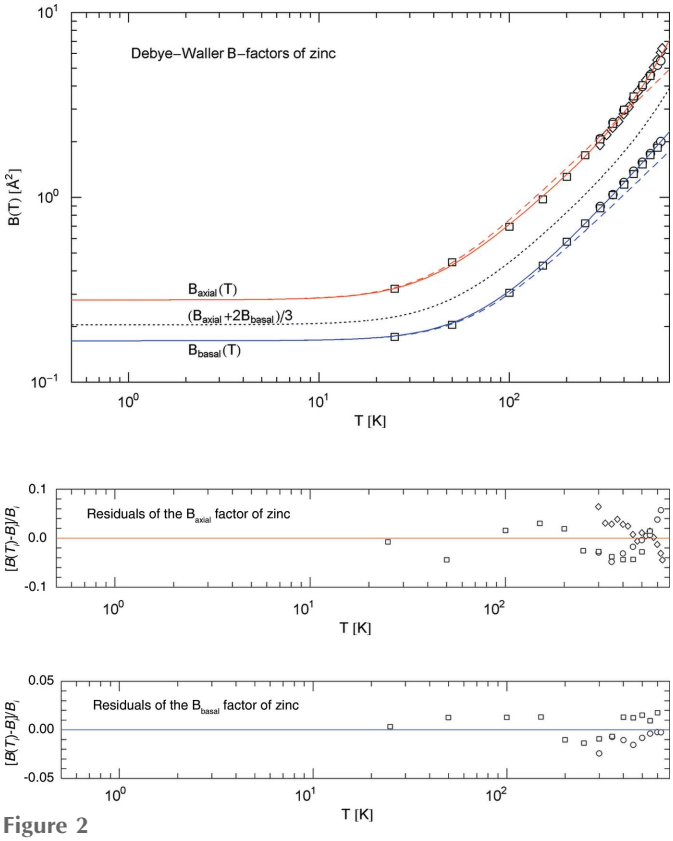


**Figure 2**
Debye–Waller $B$ factors of zinc. Data points from Skelton & Katz (1968) (squares) and Pathak & Desai (1981) (circles) were obtained by X-ray diffraction. Mössbauer $\gamma$-ray diffraction data (diamonds) are from Albanese *et al.* (1976). The $B$ factors $B_{\mathrm{axial}}(T)$ (red solid curve) and $B_{\mathrm{basal}}(T)$ (blue solid curve) are defined by the mean-squared atomic displacements $\langle u^2_{\mathrm{axial}}(T)\rangle$ (parallel to the hexagonal axis) and $\langle u^2_{\mathrm{basal}}(T)\rangle$ in the basal plane, *cf.* Section 4.2. The black dotted curve depicts the averaged factor $(B_{\mathrm{axial}} + 2B_{\mathrm{basal}})/3$. The least-squares regression is performed with the analytic fit function $B_j(T)$ in (13); the fitting parameters of the axial and basal $B$ factors are listed in Table 3. The red and blue dashed curves show the Debye approximations, obtained by dropping the quadratic and cubic terms in (13). The regressed $B_{\mathrm{axial}}(T)$, $B_{\mathrm{basal}}(T)$ and the varying Debye temperatures in Fig. 5 determine the effective oscillator masses $m_{\mathrm{eff,axial}}(T)$ and $m_{\mathrm{eff,basal}}(T)$ of normal vibrations orthogonal and parallel to the basal plane, *cf.* (19) and Fig. 8. The zero-point internal energy (see Fig. 4) is inferred from the zero-temperature limits of the $B$ factors, *cf.* (14) and Table 3. Residuals of the least-squares fits are shown in the lower panels.

**Table 2**
Isochoric heat capacity $C_V(T)$, thermal energy $U_{\rm therm}(T)$ and entropy $S(T)$ of the zinc structure at selected temperatures below the melting point.

The listed values of $C_V(T)$ are calculated from the regressed broken power law (11) with parameters in Table 1. $U_{\rm therm}$ and $S$ are obtained by integrating $C_V(T)$, *cf.* Section 2.2. Also recorded is the deviation of the Debye approximations $C_{V,\rm D}(T)$, $U_{\rm therm,D}(T)$, $S_{\rm D}(T)$ from the empirical values. $C_{V,\rm D}$ is calculated via (12), $U_{\rm therm,D}$ and $S_{\rm D}$ by integrating $C_{V,\rm D}$, see Sections 2.2, 4.1 and 4.6. The maximal relative deviations are indicated in the captions of Figs. 1 and 4.

| $T$ (K) | $C_V$ [J (K mol)$^{-1}$] | $C_V - C_{V,\rm D}$ [J (K mol)$^{-1}$] | $U_{\rm therm}$ (J mol$^{-1}$) | $U_{\rm therm} - U_{\rm therm,D}$ (J mol$^{-1}$) | $S$ [J (K mol)$^{-1}$] | $S - S_{\rm D}$ [J (K mol)$^{-1}$] |
|---|---|---|---|---|---|---|
| 5 | 0.009276 | $1.487 \times 10^{-3}$ | 0.01069 | $9.551 \times 10^{-4}$ | 0.002814 | $2.174 \times 10^{-4}$ |
| 10 | 0.1478 | 0.08547 | 0.2887 | 0.1329 | 0.03636 | 0.01559 |
| 25 | 3.237 | 2.268 | 20.94 | 14.86 | 1.087 | 0.7633 |
| 50 | 10.86 | 4.856 | 199.9 | 113.9 | 5.741 | 3.403 |
| 75 | 16.05 | 4.222 | 541.9 | 230.3 | 11.22 | 5.299 |
| 100 | 19.06 | 3.141 | 984.2 | 322.0 | 16.29 | 6.362 |
| 200 | 23.16 | 1.050 | 3151 | 507.1 | 31.15 | 7.728 |
| 298 | 24.10 | 0.4961 | 5476 | 578.0 | 40.60 | 8.024 |
| 400 | 24.47 | 0.2787 | 7956 | 616.0 | 47.75 | 8.135 |
| 500 | 24.63 | 0.1787 | 10411 | 638.3 | 53.23 | 8.185 |
| 600 | 24.73 | 0.1239 | 12880 | 653.2 | 57.73 | 8.212 |
| 692.7 | 24.78 | 0.09267 | 15175 | 663.1 | 61.29 | 8.228 |

the Debye approximation; the deviation $C_V(T) - C_{V,\rm D}(T)$ is listed in Table 2, for a few selected temperatures.

### 4.2. *B* factors of lattice vibrations parallel and perpendicular to the hexagonal axis

The Debye–Waller $B$ factor of zinc defined by vibrations along the principal axis perpendicular to the basal plane is denoted by $B_{\rm axial} = 8\pi^2\langle u^2_{\rm axial}(T)\rangle$ and the $B$ factor of vibrations parallel to the basal plane by $B_{\rm basal} = 8\pi^2\langle u^2_{\rm basal}(T)\rangle$, *cf.* (4). Thus, relating to the notation of Sections 2 and 3, $B_1 =: B_{\rm axial}$, $B_2 = B_3 =: B_{\rm basal}$, and analogous identifications are made for other quantities such as basal and axial Debye temperatures, $\theta_1 =: \theta_{\rm axial}$ and $\theta_2 = \theta_3 =: \theta_{\rm basal}$. We use X-ray and Mössbauer $\gamma$-ray diffraction data of the $B_{\rm axial}$ and $B_{\rm basal}$ factors (Skelton & Katz, 1968; Albanese *et al.*, 1976; Pathak & Desai, 1981) and perform least-squares fits with the fit function $B_j(T) = 8\pi^2\langle u^2_j(T)\rangle$, where $j$ can take the values 'axial' and 'basal', and

$$\langle u^2_j(T)\rangle = \frac{3}{m}\frac{\hbar^2 T}{k_{\rm B}\theta^2_{{\rm X},j}}\left[D_1(\theta_{{\rm X},j}/T) + \frac{1}{4}\frac{\theta_{{\rm X},j}}{T}\right] + m_{2,j}T^2 + m_{3,j}T^3. \tag{13}$$

A similar fit function was used by Shepard *et al.* (1998) for the $B$ factors of alkali halides; see also Martin & O'Connor (1978*b*). In equation (13), $m$ = 65.38 u is the atomic mass of zinc, and the Debye function $D_1(d)$ is defined in (4). The fitting parameters $\theta_{{\rm X},j}$, $m_{2,j}$ and $m_{3,j}$ are recorded in Table 3, the subscript $j$ labeling axial and basal components as defined above. Debye temperatures inferred from X-ray (or $\gamma$-ray) diffraction are marked with a subscript X. The regressed $B$ factors $B_{\rm axial}$ and $B_{\rm basal}$ are depicted in Fig. 2. We also note $3\hbar^2/({\rm u}k_{\rm B})$ = 145.526 Å$^2$K, to be substituted in (13), which gives $\langle u^2_j(T)\rangle$ (Å$^2$) in terms of $m$ (u), $\theta_{{\rm X},j}$ (K), $T$ (K), $m_{2,j}$ (Å$^2$ K$^{-2}$) and $m_{3,j}$ (Å$^2$ K$^{-3}$).

If the quadratic and cubic terms in (13) are dropped, we obtain the $B$ factors of the Debye approximation [with constant $\theta_j = \theta_{{\rm X},j}$ and $m_{{\rm eff},j} = m$ in (4)], which are also depicted in Fig. 2. The low-temperature limits of the mean-squared vibrations $\langle u^2_j(T)\rangle$ in (4) (with constant mass and Debye temperature) are constant, and the high-temperature limits are linear in temperature since $D_1(x \to 0) \sim 1$. The $B_j(T)$ in (13) (with $j$ = axial, basal) cover the full temperature range up to the melting point; the zero-temperature limits $B_j(0)$ are listed in Table 3.

In Fig. 3, we plot the Index functions ${\rm Index}[B_j(T)] = TB'_j(T)/B_j(T)$ of the axial and basal $B$ factors, together with the Index of their Debye approximations. The Index functions quantify the log–log slope of the $B$-factor curves in Fig. 2. That is, a tangent to the $B$-factor plots in Fig. 2 represents a power

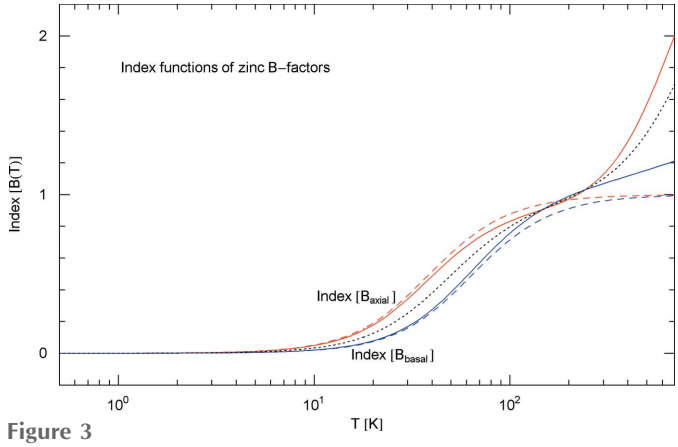


**Figure 3**
Index functions of the $B$ factors of zinc. Depicted are the log–log slopes ${\rm Index}[B_j(T)] = TB'_j(T)/B_j(T)$ of the $B_j(T)$ factors ($j$ = axial, basal) in Fig. 2. The red/blue solid curves show the slope of the axial/basal $B$ factors at the respective temperature, and the red/blue dashed curves are the slopes of their Debye approximations, *cf.* the end of Section 4.2. The black dotted curve depicts the Index of the averaged $B$ factor in Fig. 2. Intervals in which the Index curves are constant imply power-law scaling with the respective Index as exponent. Below 10 K, the $B$ factors are constant. The depicted temperature range is cut off at the melting point (in all figures). Close to the melting point at 692.73 K, the Debye approximations scale linearly with temperature, whereas the slopes of the empirical $B$ factors increase with temperature, reaching 2 (axial) and 1.2 (basal) at the melting point. The inclusion of a cubic term in the axial $B$ factor (13) substantially improves the $\chi^2$ of the fit (in contrast to the basal $B$ factor, *cf.* Table 3); the slope below the melting point does not exceed 2 despite the cubic term.

**Table 3**
Fitting parameters of the Debye–Waller factors $B_j(T)$ of zinc in Fig. 2.

The index $j$ takes the values 'axial' and 'basal,' referring to normal vibrations along the hexagonal axis and in the basal plane, *cf.* Section 4.2. The least-squares fits are performed with $B_j(T)$ in (13), depending on the listed parameters $\theta_{X,j}$, $m_{2,j}$ and $m_{3,j}$. Also recorded are the zero-temperature limits of $B_{axial}$ and $B_{basal}$. The goodness-of-fit parameters $\chi^2$/d.o.f., SE and $R^2$ are defined as in the caption of Table 1, with obvious replacements.

| $j$ | $\theta_{X,j}$ (K) | $m_{2,j}$ (Å$^2$ K$^{-2}$) | $m_{3,j}$ (Å$^2$ K$^{-3}$) | $B_j(T=0)$ (Å$^2$) | $\chi^2$ | d.o.f. | SE | $R^2$ |
|---|---|---|---|---|---|---|---|---|
| Axial | 157.44 | $-7.1973 \times 10^{-8}$ | $1.8786 \times 10^{-10}$ | 0.2791 | 0.0321 | 35 − 3 | 0.110 | 0.995 |
| Basal | 262.05 | $1.3034 \times 10^{-8}$ | 0 | 0.1677 | 0.00301 | 21 − 2 | 0.0142 | 0.9994 |

law $\propto T^{\alpha}$ whose exponent $\alpha$ is the slope of the tangent line (in the log–log coordinates of Fig. 2) given by the Index function. Thus, if the temperature dependence of the $B$ factor can be approximated in an interval by a power law, then the Index curve is nearly constant in this interval, with a value close to the power-law exponent.

### 4.3. Zero-point internal energy of the zinc structure

The zero-point energy of the lattice vibrations is calculated from the zero-temperature limits of the $B$ factors via (10),

$$U_0\,(\mathrm{J\ mol^{-1}}) = 3.27662 \times 10^{11}\,\frac{c_{V0}}{m^4}\,\frac{1/B_{axial}(0) + 2/B_{basal}(0)}{B^3_{axial}(0) + 2B^3_{basal}(0)}. \quad (14)$$

The $B$ factors at $T = 0$ are listed in Table 3. As for units, $c_{V0}$ [J (K$^4$ mol)$^{-1}$], $B_j$ (Å$^2$), $m$ (u), and we used $\hbar^2/(\mathrm{u}k_B) = 48.50875$ Å$^2$K to obtain the numerical factor in (14). The constant $c_{V0}$ is the amplitude of the low-temperature heat capacity, *cf.* the beginning of Section 3, to be identified with the fitting parameter $b_0$ in (11) and Table 1. The zero-point energy of zinc consistent with the measured $B$ factors is thus $U_0 = 556.3$ J mol$^{-1}$.

The zero-point energy of the Debye approximation, *cf.* after (12), is by a factor $U_{0,D}/U_0 = 5.29$ larger than $U_0$ obtained from $B$-factor measurements. While the zero-point lattice energy is not accessible by caloric measurement of energy differences, the thermal energy $U_{therm}(T) = U(T) - U_0$ can be obtained empirically by integrating the measured heat capacity, *cf.* Section 2.2, and a plot thereof is depicted in Fig. 4. The maximal relative deviation of $U_{therm}(T)$ from the Debye approximation $U_{therm,D}(T) = U_D(T) - U_{0,D}$ happens at 23.45 K and is substantial, $U_{therm}/U_{therm,D} = 3.46$ at this temperature (see also the captions to Figs. 1 and 4 and Section 4.6). In view of this, the large $U_{0,D}/U_0$ ratio is not surprising. The zero-point internal energy stems from the second term in (1) and (2) and is finite because of the finite spectral cutoff. The zero-temperature limit of the spectral cutoff $\Lambda(T)$ is smaller than the constant spectral cutoff $\Lambda_D$ of the Debye theory (*cf.* Section 4.1 and Fig. 6 in Section 4.5); therefore $U_0$ is smaller than the Debye zero-point energy [*cf.* the spectral representation (2) of $U(T)$].

### 4.4. Varying axial and basal Debye temperatures

The directional Debye temperatures $\theta_j(T) = \hat{c}_j\theta(T)$ (labeled $j = 1, 2, 3$ in Section 2.2) of the zinc structure are denoted by $\theta_1 = \theta_{axial}(T)$ and $\theta_2 = \theta_3 = \theta_{basal}(T)$ as in Section 4.2. The constants $\hat{c}_j$ can be extracted from the zero-temperature limits of the $B$ factors, *cf.* (9): $\hat{c}_1 = \hat{c}_{axial} = 1$ and $\hat{c}_2 = \hat{c}_3 = \hat{c}_{basal} = B_{axial}(0)/B_{basal}(0) = 1.664$ (see Table 3).

Thus, $\theta_{axial}(T) = \theta(T)$ and $\theta_{basal}(T) = \hat{c}_{basal}\theta(T)$, where $\theta(T)$ is found by solving (5). The $\Delta$ function (5) of zinc reads [*cf.* (23)]

$$\Delta(d) = 1 - (2\log[1 - \exp(-d)] + d + 2\{2\log[1 - \exp(-\hat{c}_{basal}d)] + \hat{c}_{basal}d\}) / \{8D(d) + d + 2[8D(\hat{c}_{basal}d) + \hat{c}_{basal}d]\}, \quad (15)$$

with $d = \theta(T)/T$ and $\hat{c}_{basal}$ stated above. $\theta(T)$ is calculated as indicated in Section 2.2, $\theta(T) = T\Delta^{-1}[\frac{3}{4}TS(T)/U(T)]$. The

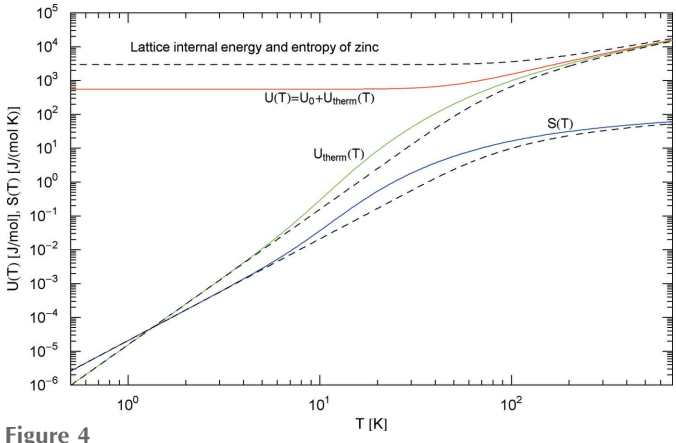


**Figure 4**
Internal energy $U(T) = \int_0^T C_V\,\mathrm{d}T + U_0$ and entropy $S(T) = \int_0^T (C_V/T)\,\mathrm{d}T$ of the zinc structure. The regressed lattice heat capacity $C_V(T)$ in the integrands is stated in (11), with fitting parameters in Table 1, see Fig. 1. The lattice energy $U(T)$, including the zero-point energy $U_0 = 556.3$ J mol$^{-1}$ [extracted from the zero-temperature limits of the measured Debye–Waller $B$ factors, *cf.* (14) and Table 3], is depicted as a red solid curve, its thermal component $U_{therm}(T) = \int_0^T C_V\,\mathrm{d}T$ as a green solid curve, and the lattice entropy as a blue solid curve. At high temperature, $U(T) \propto T$, and the entropy diverges logarithmically. The low-temperature slopes are $U_{therm}(T) \propto T^4$ and $S(T) \propto T^3$, *cf.* Section 3. The black dashed curves show the Debye approximations $U_D(T)$, $U_{therm,D}(T)$ and $S_D(T)$, based on the Debye heat capacity $C_{V,D}$ in (12) (with $\theta_D = 314.79$ K). The Debye zero-point energy of zinc, $U_{0,D} = 2944.5$ J mol$^{-1}$, see after (12), is by a factor $U_{0,D}/U_0 = 5.29$ larger than the zero-point energy consistent with the measured $B$ factors. The phonon peak in the second logarithmic temperature decade in Fig. 1 is also clearly visible in $U_{therm}(T)$ and $S(T)$. The largest relative deviation $(U_{therm} - U_{therm,D})/U_{therm}$ of the Debye approximation from the empirical thermal energy happens at 23.45 K, where $U_{therm}/U_{therm,D} = 3.46$ and $U_{therm} = 16.3$ J mol$^{-1}$. For entropy, the maximum of $(S - S_D)/S$ occurs at 24.82 K, where $S/S_D = 3.35$ and $S = 1.06$ J (K mol)$^{-1}$. The differences $U_{therm} - U_{therm,D}$ and $S - S_D$ at selected temperatures are listed in Table 2.

inversion $\Delta^{-1}$ of (15) is sketched in the Appendix, *cf.* after (30). The lattice internal energy $U(T) = \int_0^T C_V \, dT + U_0$ and entropy $S(T) = \int_0^T C_V/T \, dT$ are empirical input functions, inferred from the regressed lattice heat capacity $C_V(T)$ [*cf.* (11) and Table 1] and depicted in Fig. 4. The zero-point internal energy of zinc is $U_0 = 556.3$ J mol$^{-1}$ (*cf.* Section 4.3). The Debye temperatures $\theta_{\rm axial}(T) = \theta(T)$ and $\theta_{\rm basal}(T) = \hat{c}_{\rm basal}\theta(T)$ are plotted in Fig. 5; their zero-temperature limits coincide with the fitting parameters $\theta_{{\rm X},j}$ of the $B$ factors in Table 3, $\theta_{\rm axial}(0) = \theta_{\rm X,axial}$, $\theta_{\rm basal}(0) = \theta_{\rm X,basal}$, according to (8) and (13) [where $D_1(x \to \infty) \sim \pi^2/(6x)$].

Constant axial and basal Debye temperatures for zinc were already introduced by Grüneisen & Goens (1924). The plots of the temperature-dependent caloric and X-ray Debye temperatures of zinc reported by Barron & Munn (1967*b*), Martin (1968) and Skelton & Katz (1968) (which largely differ from one another) are not comparable with the ones in Fig. 5, since they were derived with a constant (temperature-independent) spectral cutoff. Also, these authors do not use directional Debye temperatures, but calculate one temperature-dependent Debye temperature $\theta_{\rm D}(T)$ either by comparing the Debye heat capacity (12) with the empirical heat capacity curve, or by comparing the averaged experimental $B$ factor $(B_{\rm axial} + 2B_{\rm basal})/3$ with the isotropic Debye $B$ factor obtained by dropping the quadratic and cubic terms in (13) and replacing $\theta_{{\rm X},j}$ by $\theta_{\rm D}(T)$. As mentioned, the $\theta_{\rm D}(T)$ curves obtained by these two methods substantially differ, *cf.* Skelton & Katz (1968), and a temperature-dependent Debye temperature without simultaneous variation of the spectral cutoff also violates a basic equilibrium condition (*cf.* Sections 1 and 2.2).

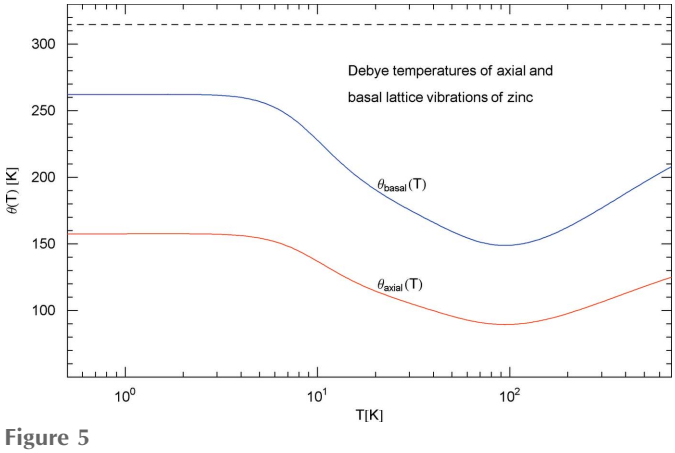


**Figure 5**
Varying Debye temperatures $\theta_{\rm axial}(T)$ and $\theta_{\rm basal}(T)$ of zinc, referring to normal vibrations along the hexagonal axis and in the basal plane. $\theta_{\rm axial}$ and $\theta_{\rm basal}$ are calculated from the temperature variation of the internal energy and entropy depicted in Fig. 4 and from the zero-temperature limits of the Debye–Waller $B$ factors in Fig. 2 and Table 3, *cf.* Section 4.4. The Debye temperatures converge to constant limit values at low and high temperature, *cf.* Section 3, but the constant high-temperature limits are not attained within the depicted temperature range of the solid phase. The horizontal dashed straight line indicates the constant Debye temperature $\theta_{\rm D} = 314.79$ K, *cf.* after (12), used in the Debye approximations in Figs. 1 and 4.

### 4.5. Temperature variation of the spectral cutoff

In contrast to the Debye temperatures $\theta_{\rm axial}(T)$ and $\theta_{\rm basal}(T)$, the cutoff factor $\Lambda(T)$ of the internal energy (1) and entropy (3) is the same for normal vibrations orthogonal and parallel to the hexagonal axis. $\Lambda(T)$ is calculated as explained in Section 2.2,

$$\Lambda(T) = \left\{\frac{(2\pi)^3}{4\pi}\frac{1}{RT}\frac{n_{\rm at}U(T)}{D(d) + d/8 + 2[D(\hat{c}_{\rm basal}d) + \hat{c}_{\rm basal}d/8]}\right\}^{1/3}, \tag{16}$$

with $U(T)$ [see after (15)] and $d = \theta(T)/T$ and $\hat{c}_{\rm basal}$ in Section 4.4. The rescaled dimensionless cutoff factor $h(T) := \Lambda(T)/n_{\rm at}^{1/3}$ is plotted in Fig. 6, where $n_{\rm at} = 6.5702 \times 10^{22}$ cm$^{-3}$ is the atomic density of zinc. $h(T)$ increases moderately with temperature, from 2.49 at zero to 3.77 at the melting point (692.7 K). Like the Debye temperatures, the cutoff depends on the zero-temperature limits of the $B$ factors, which enter via the zero-point energy (14) and $\hat{c}_{\rm basal}$. The temperature dependence of $\Lambda(T)$ compensates for the variation of $\theta(T)$, so that the equilibrium condition $\partial S/\partial U = 1/T$ is preserved (Tomaschitz, 2020*a*).

### 4.6. Internal energy and entropy components

The molar internal energy of the zinc structure can be decomposed into partial energies of normal vibrations

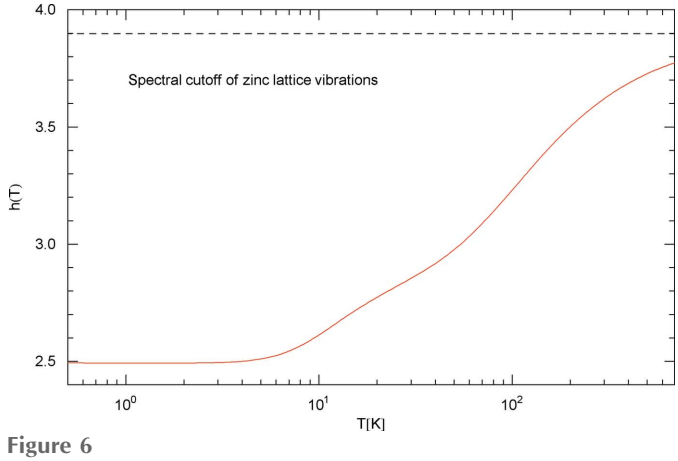


**Figure 6**
Spectral cutoff in the thermodynamic variables of zinc. The spectral cutoff $\Lambda(T) = n_{\rm at}^{1/3}h(T)$, $n_{\rm at}^{1/3} = 0.4035$ Å$^{-1}$, of the internal energy, *cf.* (1) and (2), depends on the atomic density of zinc, $n_{\rm at} = 6.5702 \times 10^{22}$ cm$^{-3}$, and a dimensionless cutoff factor $h(T)$ (red solid curve), *cf.* Section 4.5. In contrast to the axial and basal Debye temperatures of zinc depicted in Fig. 5, the spectral cutoff is the same for normal vibrations orthogonal and parallel to the basal plane. $h(T)$ is calculated from the lattice internal energy $U(T)$ of the zinc structure, *cf.* Fig. 4, and the Debye temperatures $\theta_{\rm axial}(T)$ and $\theta_{\rm basal}(T)$ by way of (16). Both the low- and high-temperature limits of $h(T)$ are constant. At high temperature, $h(T)$ converges to the constant cutoff factor of the Debye approximation, $h_{\rm D} = (6\pi^2)^{1/3}$, *cf.* after (12), indicated here as a black dashed straight line. (This convergence is not visible in the temperature range shown in this figure, as it happens above the melting point.) In the low-temperature regime, $h(T)$ depends, like $\theta_{\rm axial}$ and $\theta_{\rm basal}$, on the zero-point internal energy $U_0$, *cf.* Fig. 4.

orthogonal and parallel to the basal plane, $U(T) = U_{\rm axial} + 2U_{\rm basal}$, *cf.* (1), where

$$U_{\rm axial}(T) = \frac{4\pi}{(2\pi)^3} R \frac{\Lambda^3(T)}{n_{\rm at}} T \left\{ D[\theta_{\rm axial}(T)/T] + \frac{1}{8}\frac{\theta_{\rm axial}(T)}{T} \right\}, \tag{17}$$

and analogously for $U_{\rm basal}(T)$. The partial energies $U_{\rm axial}$ and $U_{\rm basal}$ depend on the spectral cutoff $\Lambda(T)$ and the Debye temperatures $\theta_{\rm axial}(T)$ and $\theta_{\rm basal}(T)$, respectively, calculated in Sections 4.4 and 4.5. An analogous decomposition holds for the lattice entropy, $S(T) = S_{\rm axial} + 2S_{\rm basal}$, *cf.* (3), with axial entropy component

$$S_{\rm axial}(T) = \frac{4\pi}{(2\pi)^3} R \frac{\Lambda^3(T)}{n_{\rm at}} \times \left( \frac{4}{3} D[\theta_{\rm axial}(T)/T] - \frac{1}{3}\log\{1 - \exp[-\theta_{\rm axial}(T)/T]\} \right), \tag{18}$$

and analogously for the basal component $S_{\rm basal}(T)$. $U(T)$ and $S(T)$ coincide with the empirical functions obtained from integrations of the regressed heat capacity [see after (15)] and from the zero-temperature limits of the $B$ factors determining the zero-point energy $U_0$, *cf.* Section 4.3. The temperature evolution of $U(T)$, its thermal component $U_{\rm therm} = U(T) - U_0$ and the entropy $S(T)$ are plotted in Fig. 4, together with the respective Debye approximations $U_{\rm D}(T)$, $U_{\rm therm,D} = U_{\rm D}(T) - U_{0,\rm D}$ and $S_{\rm D}(T)$. The latter are calculated by integrating the Debye heat capacity $C_{V,\rm D}(T)$ in (12) with constant Debye temperature $\theta_{\rm D} = 314.79$ K and spectral cutoff $\Lambda_{\rm D} = (6\pi^2 n_{\rm at})^{1/3}$, *cf.* Section 2.2. The differences $U_{\rm therm}(T) - U_{\rm therm,D}(T)$ and $S(T) - S_{\rm D}(T)$ are recorded in Table 2, at selected temperatures, and the maximal relative deviation of the Debye theory from the empirical $U_{\rm therm}(T)$ and $S(T)$ is indicated in the caption of Fig. 4 (and is clearly visible in this figure).

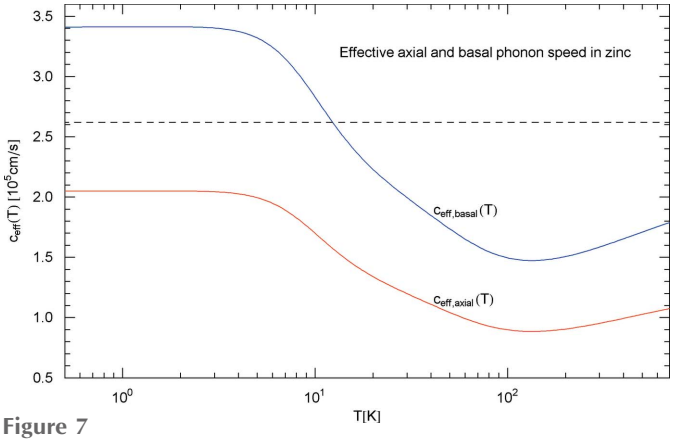


**Figure 7**
Effective phonon speed of zinc defining the temperature-dependent dispersion relations of axial and basal normal vibrations, *cf.* Section 4.7. $c_{\rm eff,axial}(T)$ refers to vibrations along the hexagonal axis and $c_{\rm eff,basal}(T)$ to vibrations in the basal plane. The constant effective phonon speed of the Debye theory, $c_{\rm eff,D} = 2.62$ km s$^{-1}$, *cf.* after (12), is indicated by the black dashed horizontal line. Since $c_{\rm eff,axial}(T) \propto \theta_{\rm axial}(T)/\Lambda(T)$ and analogously for $c_{\rm eff,basal}$, *cf.* Section 4.7, the phonon speed converges to finite limit values at low and high temperature; the constant high-temperature limits are not attained within the depicted temperature range below the melting point. For comparison, measured transversal/longitudinal sound velocities in zinc vary between 2.0 and 4.2 km s$^{-1}$ (Ledbetter, 1977).

### 4.7. Effective phonon speed and dispersion relations of axial and basal normal vibrations

The axial and basal components of the effective phonon speed are $c_{\rm eff,axial} = c_{\rm eff}(T)$ and $c_{\rm eff,basal} = \hat{c}_{\rm basal} c_{\rm eff}(T)$ (orthogonal and parallel to the basal plane, respectively), where $c_{\rm eff}(T) = k_{\rm B}\theta(T)/[\hbar\Lambda(T)]$, *cf.* Section 2.2. The Debye temperature $\theta(T)$ and the zero-temperature ratio $\hat{c}_{\rm basal} = B_{\rm axial}(0)/B_{\rm basal}(0) = 1.664$ were obtained in Section 4.4 and the spectral cutoff $\Lambda(T)$ in Section 4.5. The atomic density of zinc is $n_{\rm at} = 6.5702 \times 10^{22}$ cm$^{-3}$ (based on a mass density of 7.133 g cm$^{-3}$ and a molar mass of 65.38 g mol$^{-1}$), so that $c_{\rm eff}(T)$ (cm s$^{-1}$) = 3244.5 $\theta(T)$ (K)/$h(T)$, with dimensionless cutoff factor $h(T) = \Lambda(T)/n_{\rm at}^{1/3}$, *cf.* Section 4.5. The temperature-dependent axial and basal dispersion relations are $\omega = c_{\rm eff,axial}(T)k$ and $\omega = c_{\rm eff,basal}(T)k$, *cf.* after (2). Instead of anharmonic perturbations of the oscillator potential, we use a temperature-dependent spectral cutoff and varying Debye temperatures in the spectral representation (2), so that the dispersion relations stay linear. The effective phonon velocities $c_{\rm eff,axial}(T)$ and $c_{\rm eff,basal}(T)$ are plotted in Fig. 7.

### 4.8. Temperature variation of the effective oscillator mass of zinc

We substitute the analytic fits (13) of the mean-squared atomic displacement $\langle u_j^2(T)\rangle$ into (4) and solve for $m_{{\rm eff},j}(T)$, with index $j$ taking the values 'axial' and 'basal'. The oscillator mass of normal vibrations along the hexagonal axis is found as

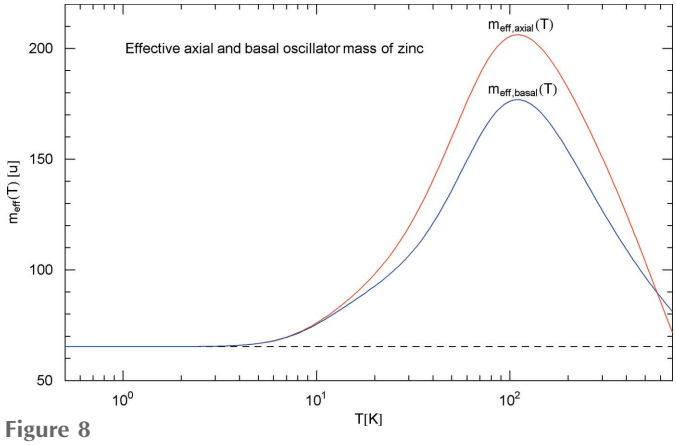


**Figure 8**
Effective oscillator mass of zinc. The curves $m_{\rm eff,axial}(T)$ and $m_{\rm eff,basal}(T)$ show the temperature-dependent effective oscillator mass of normal vibrations parallel and orthogonal to the hexagonal axis, respectively, *cf.* Section 4.8. The mass functions $m_{\rm eff,axial}(T)$, $m_{\rm eff,basal}(T)$ are calculated from the regressed $B$ factors $B_{\rm axial}(T)$, $B_{\rm basal}(T)$ in Fig. 2 and Debye temperatures $\theta_{\rm axial}(T)$, $\theta_{\rm basal}(T)$ in Fig. 5, by way of (19). The horizontal dashed line indicates the atomic mass of zinc, which is the zero-temperature limit of $m_{\rm eff,axial}(T)$ and $m_{\rm eff,basal}(T)$. The temperature range is cut off at the melting point.

$$m_{\mathrm{eff,axial}}(T)(\mathrm{u}) = \frac{145.526}{\langle u^2_{\mathrm{axial}}(T)\rangle(\mathrm{Å}^2)}\frac{T}{\theta^2_{\mathrm{axial}}(T)} \times \left\{D_1[\theta_{\mathrm{axial}}(T)/T] + \frac{1}{4}\frac{\theta_{\mathrm{axial}}(T)}{T}\right\}, \quad (19)$$

and $m_{\mathrm{eff,basal}}(T)$, the oscillator mass of basal oscillations, reads analogously. $\langle u^2_{\mathrm{axial}}(T)\rangle$ and $\langle u^2_{\mathrm{basal}}(T)\rangle$ denote the least-squares fits (13) to the empirical mean-squared vibrations, and $3\hbar^2/(\mathrm{u}k_\mathrm{B}) = 145.526$ Å$^2$K in (4). $\theta_{\mathrm{axial}}(T)$ and $\theta_{\mathrm{basal}}(T)$ are the Debye temperatures calculated in Section 4.4. At zero temperature, the effective oscillator mass coincides with the atomic mass, $m_{\mathrm{eff,axial}}(0) = m_{\mathrm{eff,basal}}(0) = m$, *cf.* Section 3. The temperature variation of $m_{\mathrm{eff,axial}}(T)$ and $m_{\mathrm{eff,basal}}(T)$ is depicted in Fig. 8.

### 4.9. Second-order *B* factors of zinc

Non-Gaussian contributions to the Debye–Waller (diffraction intensity attenuation) factors $\exp(-2M_j)$ are defined by higher-order terms in the ascending series expansion $M_j = [Q^2/(4\pi)^2](B_j + B_{2,j}Q^2 + \ldots)$, where $Q^2$ is the squared diffraction vector (Wolfe & Goodman, 1969; Day *et al.*, 1995, 1996; Shepard *et al.*, 1998, 2000; Wang *et al.*, 2017), and the subscript $j$ labels the vibrational normal components. In the case of zinc, $j$ takes the values 'axial' and 'basal,' *cf.* Section 4.2, and the diffraction vector is directed accordingly, so that we do not need to take cross-correlations into account. The leading order of $M_j$ is defined by the *B* factor $B_j(T) = 8\pi^2\langle u_j^2(T)\rangle$, *cf.* (4) and Section 4.2. The second-order coefficient $B_{2,j}(T)$ depends on the vibrational amplitude averages $\langle u_j^2(T)\rangle$ and $\langle u_j^4(T)\rangle$ via the cumulant $\kappa_j = 3\langle u_j^2(T)\rangle^2 - \langle u_j^4(T)\rangle$, $B_{2,j} = 2\pi^2\kappa_j(T)/3$. This cumulant can be expressed in terms of the Debye function $D_1$ (Tomaschitz, 2021*a*),

$$B_{2,j}(T)(\mathrm{Å}^4) = \frac{2\pi^2}{3}\left[\frac{145.526}{m_{\mathrm{eff},j}(T)}\frac{T}{\theta_j^2(T)}\right]^2 \times \left[D_1^2(d_j) + \frac{1}{2}d_jD_1(d_j) + \frac{d_j^2}{8}\right], \quad (20)$$

where we use the shortcut $d_j(T) = \theta_j(T)/T$ and $3\hbar^2/(\mathrm{u}k_\mathrm{B}) = 145.526$ Å$^2$K. $m_{\mathrm{eff},j}(T)$ is the effective mass (19) in atomic units, the Debye function $D_1$ is defined in (4), and $j =$ axial, basal. The varying Debye temperatures $\theta_j(T)$ of zinc are calculated in Section 4.4. The Debye approximation of $B_{2,j}(T)$ in (20) is obtained by replacing $m_{\mathrm{eff},j}(T)$ by the atomic mass and $\theta_j(T)$ by the constant directional Debye temperatures $\theta_{\mathrm{X},j}$ in Table 3; see also Section 4.2, where the Debye approximation of the $B_j(T)$ factors is obtained in the same way.

The second-order *B* factors (20) are related to the $B_j(T)$ factors (4) by

$$B_{2,j}(T) = \frac{1}{96\pi^2}B_j^2(T)\left[1 + \frac{d_j^2}{16D_1^2(d_j) + 8d_jD_1(d_j) + d_j^2}\right], \quad (21)$$

which is obtained by substituting the effective mass (19) into (20). The temperature evolution of the second-order factors $B_{2,\mathrm{axial}}(T)$ and $B_{2,\mathrm{basal}}(T)$ of zinc is depicted in Fig. 9, together with their Debye approximations. The Index functions $\mathrm{Index}[B_{2,j}(T)] = TB'_{2,j}(T)/B_{2,j}(T)$ [*cf.* the end of Section 4.2 and equation (31) in the Appendix] of the second-order factors are plotted in Fig. 10, representing the log–log slope of the $B_{2,j}(T)$ curves in Fig. 9.

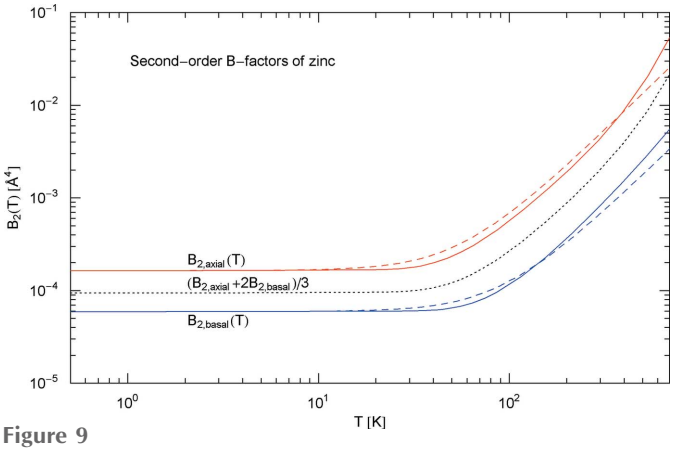


**Figure 9**
Second-order *B* factors of zinc. Depicted are the axial (red solid curve) and basal (blue solid curve) second-order *B* factors quantifying the non-Gaussian component of the Debye–Waller damping factors, *cf.* Section 4.9. The solid curves are plots of $B_{2,j}(T)$ in (21). The averaged (isotropized) second-order *B* factor $(B_{2,\mathrm{axial}} + 2B_{2,\mathrm{basal}})/3$ is indicated by the black dotted curve. The dashed curves are the Debye approximations of $B_{2,\mathrm{axial}}$ and $B_{2,\mathrm{basal}}$, *cf.* after (20), which admit quadratic power-law scaling close to the melting point. See also Fig. 10 depicting the temperature dependence of the log–log slope of these factors.

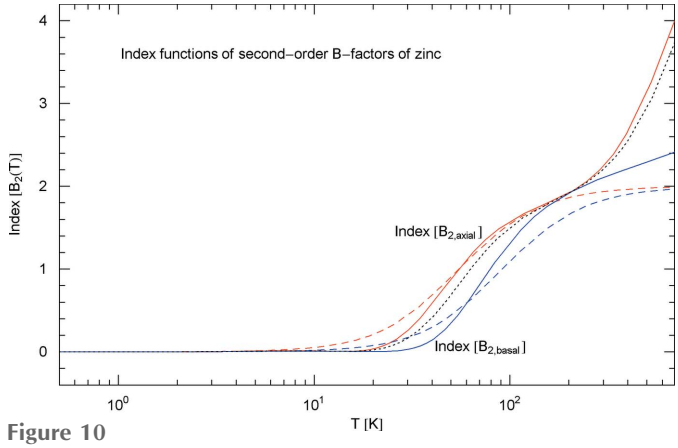


**Figure 10**
Index functions of the second-order *B* factors of zinc. The log–log slope of the axial and basal second-order *B* factors in Fig. 9 is here depicted by the Index curves $\mathrm{Index}[B_{2,j}(T)] = TB'_{2,j}(T)/B_{2,j}(T)$, *cf.* Section 4.9. The dashed curves show the slope of the Debye approximations in Fig. 9, and the black dotted curve depicts the Index function of the averaged second-order *B* factor in Fig. 9. At high temperature, the Indices are by a factor of two larger than the slopes of the Gaussian $B_j(T)$ factors in Fig. 3, because of the quadratic $B_j(T)$ dependence of the $B_{2,j}(T)$ factors, *cf.* (21) and (31). [The second temperature-dependent factor in (21) varies only moderately and decreases monotonously, being close to 2 at low temperature and close to 1 at high temperature.] Above 200 K, the slope of the axial Debye approximation (red dashed curve) is nearly constant and approximately 2, whereas the slope of $B_{2,\mathrm{axial}}(T)$ (red solid curve) varies between 2 and 4 in the 200–693 K interval.

## 5. Conclusion

We outlined a practical method to describe anisotropic lattice vibrations in elemental crystals, focusing on a specific example, the hexagonal close-packed zinc structure. The experimental lattice heat capacity, internal energy and equilibrium entropy as well as the temperature evolution of the measured $B$ factors of zinc can self-consistently be modeled, from the low-temperature regime up to the melting point, by employing the varying Debye temperatures $\theta_{\rm axial}(T)$, $\theta_{\rm basal}(T)$ (*cf.* Section 4.4), the temperature-dependent spectral cutoff $\Lambda(T)$ (*cf.* Section 4.5) and the effective oscillator masses $m_{\rm eff,axial}(T)$, $m_{\rm eff,basal}(T)$ (*cf.* Section 4.8).

In Sections 2 and 3, we sketched the general formalism for anisotropic monatomic crystals. The atomic vibrations are partitioned into normal components described by a temperature-dependent spectral cutoff $\Lambda(T)$ and directional Debye temperatures $\theta_j(T)$, the index $j$ labeling three vibrational normal components. (In the case of zinc, the two components in the basal plane are identical, and normal vibrations are labeled as axial and basal accordingly, *cf.* Section 4.) In contrast to cubic monatomic crystals, the Debye temperatures of the normal components differ in anisotropic crystals. By the way, in compound crystals, the spectral cutoffs of the normal vibrations of different atomic species also differ in general (Tomaschitz, 2021*a*).

The varying spectral cutoff and Debye temperatures can be extracted from the experimental lattice heat capacity and low-temperature Debye–Waller $B$ factors, as explained in Sections 2.2 and 3 and illustrated with zinc in Section 4. The effective phonon speed $c_{{\rm eff},j}(T)$ defining the dispersion relations of the normal vibrations is determined by the Debye temperatures $\theta_j(T)$ and spectral cutoff $\Lambda(T)$, *cf.* Sections 2.2 and 4.7. The effective oscillator density $n_{{\rm oscil},j}(T)$ of the vibrational components is calculated from the spectral cutoff, *cf.* Section 2.1, and the effective oscillator mass $m_{{\rm eff},j}(T)$ from the respective Debye–Waller factor $B_j(T)$, *cf.* Section 4.8.

We have chosen to model empirical heat capacity and $B$-factor data of anisotropic crystals by way of a temperature-dependent spectral cutoff, temperature-dependent directional Debye temperatures and effective oscillator masses. Apart from these temperature dependencies and the use of directional quantities in the case of anisotropy, there are no further changes made in the Debye theory. The harmonic oscillator potential, resulting in linear (but temperature-dependent) dispersion relations for the normal vibrations, and the uniform density of phonon states of the Debye theory are retained, which makes the described non-perturbative formalism possible.

Several other methods to account for the deviations of the Debye theory from empirical data are reviewed by Gopal (1966). Anharmonic perturbations of the oscillator potential and nonlinear phonon dispersion curves have been used by Merisalo & Larsen (1977, 1979), Field (1983), Malica & Dal Corso (2019), Ulian & Valdrè (2019). A discrete spectral component (Einstein terms) can be added to the Debye heat capacity at optical frequencies (*cf.* Meissner *et al.*, 1978; Hoser & Madsen, 2016, 2017; Sovago *et al.*, 2020). A non-uniform phonon density of states was used by Tewari & Silotia (1990) for zinc and Malica & Dal Corso (2019) for several other monatomic crystals.

The phonon peaks occurring in the lattice heat capacity of anisotropic crystals in the crossover region between the low-temperature and classical regimes largely deviate from the Debye heat capacity as exemplified by zinc in Fig. 1 and graphite (Tomaschitz, 2020*b*). The onset of the phonon peak is indicated by an inflection point in the log–log slope of the heat capacity, *cf.* Fig. 1.

When modeling heat capacity data, the preference of experimentalists seems to be the Debye theory in combination with a temperature-dependent Debye temperature, *cf. e.g.* Goetsch *et al.* (2012), Li *et al.* (2017) and references therein. In this case, the spectral cutoff has also to vary with temperature in order to satisfy the equilibrium condition $\partial S/\partial U = 1/T$, which would otherwise be violated by a varying Debye temperature (Tomaschitz, 2020*a*). This also holds true for anisotropic crystals: since the Debye temperature $\theta_j(T)$ of each vibrational normal component varies with temperature, the spectral cutoff $\Lambda(T)$ has to vary as well to ensure that the internal-energy derivative of entropy coincides with the inverse temperature. The above condition on the entropy derivative is preserved by relating $\theta_j(T)$ and $\Lambda(T)$ to the internal energy and entropy, *cf.* Section 2.2.

In contrast to the Debye theory, where the zero-point energy of the phonons is already determined by the constant Debye temperature, *cf.* Section 4.1, the zero-point energy $U_0$ emerges as a free constant in the temperature-dependent spectral cutoff $\Lambda(T)$ and Debye temperatures $\theta_j(T)$, *cf.* Section 2.2. The Debye–Waller factors $B_j(T)$ also depend on $U_0$ by way of the Debye temperatures $\theta_j(T)$, especially in the low-temperature regime, *cf.* Section 3. Therefore, the zero-point energy $U_0$, which is calorically not measurable, can be inferred from the zero-temperature limits of the measured $B$ factors, as explained in Section 3 for anisotropic crystals and specifically for zinc in Section 4.3. Finally, and again in contrast to the Debye theory, there is no need to distinguish between caloric and X-ray Debye temperatures, as the varying directional Debye temperatures $\theta_j(T)$ extracted from the empirical heat capacity are identical to those used in the modeling of the Debye–Waller $B$ factors.

## APPENDIX A
## Invertibility of the Δ function, and logarithmic derivative of second-order $B$ factors

### A1. Invertibility of $\Delta(d)$

We demonstrate that the function $\Delta(d)$ in (5),

$$\Delta(d) = \frac{\sum_j \chi_j\{4D(d_j) - \log[1-\exp(-d_j)]\}}{\sum_j \chi_j[4D(d_j)+d_j/2]},$$

$$D(d) := \frac{1}{d^3}\int_0^d \frac{x^3\,{\rm d}x}{\exp(x)-1}, \tag{22}$$

with $d_j = \hat{c}_j d$, is strictly monotonously decreasing on the positive real axis, for any choice of positive constants $\hat{c}_j$ and $\chi_j$. Here, we consider a more general function than $\Delta(d)$ stated in (5) where $\chi_j = 1$ and $j = 1, 2, 3$. Equation (22) is the generalization of $\Delta(d)$ in (5) for compound crystals (Tomaschitz, 2021*a*), where the constants $\chi_j$ depend on the atomic composition and the summation in (22) is over $j = 1, \ldots, 3N$, with $N$ atomic species in the formula unit. [$\Delta(d)$ in (5) applies to elemental crystals.]

We will show that $\Delta'(d) < 0$ for $d > 0$, which means that $\Delta(d)$ is invertible on the positive real axis, as required for the calculation of the Debye temperatures in Sections 2.2 and 4.4. Before differentiating, it is convenient to eliminate $D(d_j)$ in the numerator of (22),

$$\Delta(d) = 1 - \frac{\sum_j \chi_j\{2\log[1-\exp(-d_j)] + d_j\}}{\sum_j \chi_j[8D(d_j) + d_j]}. \tag{23}$$

Using the derivative of the Debye function in (22),

$$D'(d) = -\frac{3}{d}D(d) + \frac{1}{\exp(d)-1}, \tag{24}$$

we find that $\Delta'(d) < 0$ is equivalent to $\sum_{j,k} \hat{c}_j \chi_j \chi_k f_{jk} > 0$, with

$$\begin{aligned} f_{jk} := &\left[\frac{2}{\exp(d_j)-1} + 1\right][8D(d_k) + d_k] \\ &+ \left[\frac{24}{d_j}D(d_j) - \frac{8}{\exp(d_j)-1} - 1\right] \\ &\times \{2\log[1-\exp(-d_k)] + d_k\}, \end{aligned} \tag{25}$$

where $d_i = \hat{c}_i d$. The coefficients $f_{jk}$ are independent of the positive constants $\hat{c}_j$ and $\chi_j$. It suffices to show that $f_{jk} > 0$. To this end, we rearrange the $f_{jk}$,

$$\begin{aligned} f_{jk} = &2\left[1 + \frac{2}{\exp(d_j)-1}\right]\{4D(d_k) - \log[1-\exp(-d_k)]\} \\ &+ \frac{6}{d_j}\left[4D(d_j) - \frac{d_j}{\exp(d_j)-1}\right]\{2\log[1-\exp(-d_k)] + d_k\}, \end{aligned} \tag{26}$$

and also note two identities obtained by integration by parts,

$$D(d) - \log[1-\exp(-d)] = -\frac{3}{d^3}\int_0^d \log[1-\exp(-x)]x^2\,\mathrm{d}x > 0, \tag{27}$$

with Debye function $D(d)$ in (22), and

$$4D(d) - \frac{d}{\exp(d)-1} = \frac{1}{d^3}\int_0^d \frac{x^4\exp(x)\,\mathrm{d}x}{[\exp(x)-1]^2} > 0. \tag{28}$$

Because of the positivity of the expressions (27) and (28), it is evident that the condition $f_{jk} > 0$ with $f_{jk}$ in (26) is equivalent to the inequality $\psi(d_j) + \varphi(d_k) > 0$, where

$$\begin{aligned} \psi(d_j) &:= \frac{d_j}{3}\frac{1 + 2/[\exp(d_j)-1]}{4D(d_j) - d_j/[\exp(d_j)-1]}, \\ \varphi(d_k) &:= \frac{2\log[1-\exp(-d_k)] + d_k}{4D(d_k) - \log[1-\exp(-d_k)]}. \end{aligned} \tag{29}$$

We consider $\psi(d_j)$ and $\varphi(d_k)$ as two functions of independent variables $d_j$ and $d_k$ on the positive real axis. $\psi(d_j)$ is positive for $d_j \geq 0$ and attains its minimum at $d_j = 0$, $\psi(0) = 2$. By the way, the asymptotic limits of the Debye function in (22) are

$$D(d) = \frac{1}{3} - \frac{d}{8} + \frac{d^2}{60} - \mathrm{O}(d^4),\ D(d) = \frac{\pi^4}{15}\frac{1}{d^3} + \mathrm{O}[\exp(-d)]. \tag{30}$$

The numerator of $\varphi(d_k)$ in (29) has a zero at $\tilde{d}_k = -\log\{[3-(5)^{1/2}]/2\} \simeq 0.96$. $\varphi(d_k)$ is positive for $d_k > \tilde{d}_k$. In the range $0 \leq d_k < \tilde{d}_k$, $\varphi(d_k)$ is negative and attains its minimum at $d_k = 0$, $\varphi(0) = -2$. Both functions $\psi(d_j)$ and $\varphi(d_k)$ in (29) increase monotonously on the positive real axis. Thus the inequality $\psi(d_j) + \varphi(d_k) > 0$ holds true for independent variables $d_j$ and $d_k$ on the positive real axis, and equality is only attained at $d_j = d_k = 0$. Since $\psi(d_j) + \varphi(d_k) > 0$ is equivalent to $f_{jk} > 0$, *cf.* (25) and (26), the derivative of $\Delta(d)$ in (22) and (23) is negative along the positive real axis, irrespective of the choice of positive constants $\hat{c}_j$ and $\chi_j$, so that $\Delta(d)$ is invertible.

As for the practical inversion of $\Delta(d)$ in (5) [or (15) in the case of zinc], the asymptotic limits of $\Delta(d)$ [calculated by substituting (30)] can be inverted analytically. The inversion in the crossover region (typically stretching over two or three logarithmic decades) is done numerically. First, we determine the numerical values of the parameters $\hat{c}_j$ in (5) from the zero-temperature limits of the empirical Debye–Waller $B$ factors, *cf.* (9) and Section 4.4, so that $\Delta(d)$ only depends on the variable $d$. In the crossover interval, we choose a descending sequence of closely spaced and logarithmically equidistributed points $p_n$ and generate a table of function values $[p_n, \Delta(p_n)]$. The inverse of $\Delta(d)$ in the crossover region is approximated by a cubic polynomial interpolation of the function values defined by the inverted table $[\Delta(p_n), p_n]$.

### A2. Logarithmic derivative of $B_{2,j}(T)$

The numerical evaluation of the Index function [see after (21) and Fig. 10] of the second-order $B$ factors $B_{2,j}(T)$ in (21) is done with the logarithmic derivative

$$\begin{aligned} \frac{B'_{2,j}(T)}{B_{2,j}(T)} = &2\frac{B'_j(T)}{B_j(T)} + \frac{d_j d'_j(T)}{8D_1^2(d_j) + 4d_j D_1(d_j) + d_j^2} \\ &\times \left\{1 + \frac{4D_1(d_j) + d_j}{16D_1^2(d_j) + 8d_j D_1(d_j) + d_j^2}\right. \\ &\left.\times \left[4D_1(d_j) - d_j - \frac{4d_j}{\exp(d_j)-1}\right]\right\}, \end{aligned} \tag{31}$$

obtained by using the identity $D'_1(x) = -D_1(x)/x + 1/[\exp(x)-1]$ for the Debye function $D_1(x)$ in (4). Here, $d_j = \hat{c}_j d$, with $d = \theta(T)/T$, as in (20) and (22). [We also note $d_j(T) = \theta_j(T)/T$ with $\theta_j = \hat{c}_j\theta(T)$, *cf.* Sections 2.2 and 4.9.] $B'_j(T)$ is the derivative of the regressed $B$ factors in (13), and

the Debye temperatures $\theta_j(T)$ of zinc are calculated in Section 4.4.

The derivative $d'_j(T) = \hat{c}_j d'(T)$ in (31) is found by differentiating the equation $\Delta(d) = \frac{3}{4}TS/U$ in (5), with the $\Delta$ function of zinc in (15),

$$d'(T) = \frac{3}{4}\left[\frac{TS(T)}{U(T)}\right]' \frac{1}{\Delta'(d)}. \qquad (32)$$

The internal energy $U(T)$ and entropy $S(T)$ are calculated from the regressed heat capacity and the zero-temperature limits of the $B_j(T)$ factors, *cf.* Section 4.4. The derivatives in (32) can be done analytically, using the integral representations of $U(T)$ and $S(T)$ in Section 4.4 and also the identity (24) for $D'(d)$ when differentiating $\Delta(d)$ in (15). This way to obtain the derivative $d'(T)$ [or $\theta'(T)$] is preferable to direct numerical differentiation of $d(T) = \Delta^{-1}(\frac{3}{4}TS/U)$, since the inverted $\Delta$ function is approximated by an interpolated function as pointed out above.

## References


Albanese, G., Deriu, A. & Ghezzi, C. (1976). *Acta Cryst.* A**32**, 904–909.
Altmann, S. L. & Bradley, C. J. (1965). *Rev. Mod. Phys.* **37**, 33–45.
Arblaster, J. W. (2018). *Selected Values of the Crystallographic Properties of Elements.* Materials Park, Ohio: ASM International.
Barron, T. H. K. & Munn, R. W. (1967*a*). *Acta Cryst.* **22**, 170–173.
Barron, T. H. K. & Munn, R. W. (1967*b*). *Philos. Mag.* **15**, 85–103.
Butt, N. M., Bashir, J., Willis, B. T. M. & Heger, G. (1988). *Acta Cryst.* A**44**, 396–398.
Cetas, T. C., Holste, J. C. & Swenson, C. A. (1969). *Phys. Rev.* **182**, 679–685.
Day, J. T., Mullen, J. G. & Shukla, R. C. (1995). *Phys. Rev. B*, **52**, 168–176.
Day, J. T., Mullen, J. G. & Shukla, R. C. (1996). *Phys. Rev. B*, **54**, 15548–15549.
Eichenauer, W. & Schulze, M. (1959). *Z. Naturforsch. A*, **14**, 28–32.
Field, D. W. (1983). *Phys. Status Solidi A*, **77**, 733–740.
Garland, C. W. & Silverman, J. (1961). *J. Chem. Phys.* **34**, 781–782.
Goetsch, R. J., Anand, V. K., Pandey, A. & Johnston, D. C. (2012). *Phys. Rev. B*, **85**, 054517.
Gopal, E. S. R. (1966). *Specific Heats at Low Temperatures.* New York: Plenum.
Grønvold, F. & Stølen, S. (2002). *Thermochim. Acta*, **395**, 127–131.
Grüneisen, E. & Goens, E. (1924). *Z. Phys.* **29**, 141–156.
Hoser, A. A. & Madsen, A. Ø. (2016). *Acta Cryst.* A**72**, 206–214.
Hoser, A. A. & Madsen, A. Ø. (2017). *Acta Cryst.* A**73**, 102–114.
Killean, R. C. G. & Lisher, E. L. (1975). *J. Phys. F Met. Phys.* **5**, 1107–1112.
Kumpat, G. & Rossmanith, E. (1990). *Acta Cryst.* A**46**, 413–422.
Ledbetter, H. M. (1977). *J. Phys. Chem. Ref. Data*, **6**, 1181–1203.
Li, Z. W., Guo, H., Hu, Z., Chan, T. S., Nemkovski, K. & Komarek, A. C. (2017). *Phys. Rev. Mater.* **1**, 044005.
Malica, C. & Dal Corso, A. (2019). *Acta Cryst.* A**75**, 624–632.
Martin, C. J. & O'Connor, D. A. (1978*a*). *Acta Cryst.* A**34**, 500–505.
Martin, C. J. & O'Connor, D. A. (1978*b*). *Acta Cryst.* A**34**, 505–512.
Martin, D. L. (1968). *Phys. Rev.* **167**, 640–651.
Martin, D. L. (1969). *Phys. Rev.* **186**, 642–648.
Meissner, M., Tausend, A. & Wobig, D. (1978). *Phys. Status Solidi A*, **49**, 59–66.
Merisalo, M. & Larsen, F. K. (1977). *Acta Cryst.* A**33**, 351–354.
Merisalo, M. & Larsen, F. K. (1979). *Acta Cryst.* A**35**, 325–327.
Mizutani, U. (1971). *Jpn. J. Appl. Phys.* **10**, 367–369.
Pathak, P. D. & Desai, R. J. (1981). *Phys. Status Solidi A*, **64**, 741–745.
Peng, L.-M., Dudarev, S. L. & Whelan, M. J. (2004). *High-Energy Electron Diffraction and Microscopy.* Oxford: Oxford University Press.
Peng, L.-M., Ren, G., Dudarev, S. L. & Whelan, M. J. (1996). *Acta Cryst.* A**52**, 456–470.
Phillips, N. E. (1958). *Phys. Rev. Lett.* **1**, 363–365.
Rossmanith, E. (1977). *Acta Cryst.* A**33**, 593–601.
Rossmanith, E. (1984). *Acta Cryst.* B**40**, 244–249.
Seidel, G. & Keesom, P. H. (1958). *Phys. Rev.* **112**, 1083–1088.
Shepard, C. K., Mullen, J. G. & Schupp, G. (1998). *Phys. Rev. B*, **57**, 889–897.
Shepard, C. K., Mullen, J. G. & Schupp, G. (2000). *Phys. Rev. B*, **61**, 8622–8624.
Skelton, E. F. & Katz, J. L. (1968). *Phys. Rev.* **171**, 801–808.
Sovago, I., Hoser, A. A. & Madsen, A. Ø. (2020). *Acta Cryst.* A**76**, 32–44.
Tewari, S. P. & Silotia, P. (1990). *J. Phys. Condens. Matter*, **2**, 7743–7751.
Tomaschitz, R. (2017). *Physica A*, **483**, 438–455.
Tomaschitz, R. (2020*a*). *Physica B*, **593**, 412243.
Tomaschitz, R. (2020*b*). *Appl. Phys. A*, **126**, 102.
Tomaschitz, R. (2020*c*). *Physica A*, **541**, 123188.
Tomaschitz, R. (2021*a*). *J. Phys. Chem. Solids*, **152**, 109773.
Tomaschitz, R. (2021*b*). *Phys. Lett. A*, **393**, 127185.
Tomaschitz, R. (2021*c*). *Eur. Phys. J. Plus*, **136**, 629.
Ulian, G. & Valdrè, G. (2019). *Acta Cryst.* B**75**, 1042–1059.
Wang, K., Huang, X., Li, J., Xu, Q., Dan, J. & Ren, X. (2017). *Acta Cryst.* A**73**, 151–156.
Wolfe, G. A. & Goodman, B. (1969). *Phys. Rev.* **178**, 1171–1189.
Zimmerman, J. E. & Crane, L. T. (1962). *Phys. Rev.* **126**, 513–516.